Published in final edited form as:
J Magn Reson. 2013 April ; 229: 116–126. doi:10.1016/j.jmr.2012.11.029.

Magnetic Particle Imaging (MPI) for NMR and MRI Researchers

Emine U. Saritas,
Department of Bioengineering, University of California, Berkeley, Berkeley, CA 94720-1762 USA, saritas@berkeley.edu

Patrick W. Goodwill,
Department of Bioengineering, University of California, Berkeley, Berkeley, CA 94720-1762 USA

Laura R. Croft,
Department of Bioengineering, University of California, Berkeley, Berkeley, CA 94720-1762 USA

Justin J. Konkle,
Department of Bioengineering, University of California, Berkeley, Berkeley, CA 94720-1762 USA

Kuan Lu,
Department of Bioengineering, University of California, Berkeley, Berkeley, CA 94720-1762 USA

Bo Zheng, and
Department of Bioengineering, University of California, Berkeley, Berkeley, CA 94720-1762 USA

Steven M. Conolly
Departments of Bioengineering and EECS, University of California, Berkeley, Berkeley, CA 94720-1762 USA

Abstract

Magnetic Particle Imaging (MPI) is a new tracer imaging modality that is gaining significant interest from NMR and MRI researchers. While the physics of MPI differ substantially from MRI, it employs hardware and imaging concepts that are familiar to MRI researchers, such as magnetic excitation and detection, pulse sequences, and relaxation effects. Furthermore, MPI employs the same superparamagnetic iron oxide (SPIO) contrast agents that are sometimes used for MR angiography and are often used for MRI cell tracking studies. These SPIOs are much safer for humans than iodine or gadolinium, especially for chronic kidney disease (CKD) patients. The weak kidneys of CKD patients cannot safely excrete iodine or gadolinium, leading to increased morbidity and mortality after iodinated X-ray or CT angiograms, or after gadolinium MRA studies. Iron oxides, on the other hand, are processed in the liver, and have been shown to be safe even for CKD patients. Unlike the “black blood” contrast generated by SPIOs in MRI due to increased T_2^* dephasing, SPIOs in MPI generate positive, “bright blood” contrast. With this ideal contrast, even prototype MPI scanners can already achieve fast, high-sensitivity, and high-contrast angiograms with millimeter-scale resolutions in phantoms and in animals. Moreover, MPI shows great potential for an exciting array of applications, including stem cell tracking *in vivo*, first-pass contrast studies to diagnose or stage cancer, and inflammation imaging *in vivo*. So far, only a handful of prototype small-animal MPI scanners have been constructed worldwide. Hence, MPI is

Correspondence to: Emine U. Saritas.

open to great advances, especially in hardware, pulse sequence, and nanoparticle improvements, with the potential to revolutionize the biomedical imaging field.

Keywords

Magnetic Particle Imaging; MPI; Magnetic Nanoparticles; Superparamagnetic Iron Oxide; SPIO; Angiography; Stem Cell Tracking

1. Introduction

A new tracer imaging modality called Magnetic Particle Imaging (MPI) was first presented in 2005 by Gleich and Weizenecker [1]. Seven years later, MPI is now at an exciting stage of development similar to where MRI was in the early 1980s, when commercial MRI scanners and contrast agents were just being developed and the *k*-space analysis [2, 3] had just emerged as the common conceptual framework for all MRI. Although currently only a handful of prototype small animal MPI scanners have been constructed worldwide, there is significant interest in this new imaging modality, especially from NMR and MRI researchers. In recent years, steady progress has been made with pre-clinical imaging results in phantoms and mice. These results already show promise for a variety of biomedical applications, including kidney-safe angiograms, stem cell tracking *in vivo*, contrast studies to diagnose and stage cancer, and inflammation imaging *in vivo*.

Medical Motivation for MPI: We lack a Safe Contrast Agent for CKD Patients

The three leading causes of death in the USA are cardiovascular disease (25% of all deaths), cancer (23%), and stroke (5%) [4]. The diagnosis and treatment planning for each of these diseases relies on angiographic methods, including X-ray angiography, CT angiography (CTA), and MR angiography (MRA). In 2003, over 80 million intravascular contrast media injections were administered worldwide [5], dominated by X-ray and CTA using iodinated contrast. In 2004 there were 3 million coronary angiograms, 26 million CTAs, and 2 million X-ray angiograms in the USA alone [6].

A serious clinical challenge is performing safe angiograms on Chronic Kidney Disease (CKD) patients. CKD is a progressive loss of renal function, with stage 5 CKD patients needing dialysis or transplantation to survive. Currently, 13% of the US adults have CKD, and fully 47% of patients over age 70 have CKD. Because CKD patients skew to older populations, *CKD patients now represent 25% of patients who present to the X-ray angiography suite* [7, 8]. The problem is that their kidneys cannot safely excrete our two contrast agents, iodine and gadolinium. *Stage 4 and 5 CKD patients have up to a 30% to 40% risk of contrast-induced nephropathy (CIN) from an iodinated contrast injection.* CIN is a severe reduction in kidney function induced by a contrast agent, and CIN incurs a 2% to 8% risk of requiring dialysis [9]. In patients requiring dialysis after X-ray angiography, the 1-year mortality rate is worse than 55%, a significant increase from 6% rate for those who did not require dialysis [10]. Gadolinium-MRA is now contraindicated for late-stage CKD patients due to the risk of Nephrogenic Systemic Fibrosis (NSF) [11–14]. As the population ages, the number of high-risk CKD (Stage 3 or above) patients will certainly increase. Hence, it is clear that CKD patients will benefit greatly from a safer contrast agent with quantitative, positive contrast.

While CT necessarily requires iodine contrast agent, MRI researchers have been actively looking for methods safer than Gadolinium-MRA. Safer MRA possibilities include non-contrast MRA 4 pulse sequences [15–17] and MRA using super-paramagnetic iron oxide (SPIO) contrast agents [18]. SPIO contrast agents are processed in the liver rather than the

kidneys [19, 20], and have been shown to be safe for CKD patients [21]. However, the voxels containing SPIOs appear dark due to T2* dephasing, yielding "black blood" contrast. This negative contrast mechanism makes it difficult to quantify lumen area or the precise location of SPIOs. Non-contrast MRA methods, on the other hand, have reduced contrast and robustness when compared to contrast-based MRA. Hence, MRA with SPIOs and non-contrast MRA methods have not been as clinically popular as gadolinium-based MRA.

Magnetic Particle Imaging (MPI) [1, 22–27] employs the same kidney-safe SPIO contrast agents that are only rarely used in MRI angiography. With these contrast agents, MPI has already been demonstrated experimentally to obtain fast, high-sensitivity, and high-contrast angiograms in phantoms and in animals with ideal "bright blood" contrast. As shown in Fig. 1, our X-space FFP and projection (FFL) MPI imagers (discussed in detail in Section 3) already demonstrate millimeter-scale resolutions with high contrast and sensitivity.

MPI for NMR/MRI researchers

The link between NMR and Magnetic Particle Imaging extends beyond magnetic excitation and detection. NMR and MRI researchers will see that MPI employs familiar concepts and hardware such as magnetic field gradients, homogeneous transmit and receiver coils, pulse sequences, relaxation effects, and the reciprocity principle. Just as in MRI scanners, MPI scanners must also prevent both overheating of patients (specific absorption rate, or SAR) and peripheral nerve stimulation (PNS). One compelling reason for NMR/MRI specialists to delve into Magnetic Particle Imaging is the *enormous* boost of magnetization. The nuclear paramagnetic susceptibility of water in MRI is only 3.8 parts-per-billion at 37°C [28], which translates to a weak NMR magnetization ($\mu_0 M_0$ = 27 nT at 7 T). The magnetization detected by MPI is electronic superparamagnetism, and is about 600 mT in intensity [29], *which is 22 million times stronger than the MRI magnetization at 7 T.* Of course, MRI enjoys much higher concentrations of *in vivo* water (55 molar), and paramagnetic agents (e.g., 1 mM Gadolinium in bolus) can improve the signal-to-noise ratio (SNR) efficiency by an order of magnitude. Nevertheless, the enormous boost in magnetization ought to enable MPI to compete with MRI angiograms even when using kidney-safe tracers at extremely low concentration (perhaps sub-micromolar) with excellent contrast-to-noise ratios.

2. Imaging in MPI: Analogs between *k*-space and x-space

The physics of MPI differ substantially from MRI. In MPI, a sensitive point is rapidly rastered across the sample to produce a tomographic image, as demonstrated in Fig. 2. To produce the sensitive point, MPI takes advantage of the nonlinear magnetization response of SPIOs to applied magnetic fields. As shown in Fig. 2a, the magnetization of SPIOs is nonlinear with the applied field and converges to saturation above a certain threshold. Hence, in the presence of a strong magnetic field gradient as the one shown in Fig. 2b, the SPIOs are considered to be "saturated" at every point except for at the sensitive point, called the "Field Free Point" (FFP). When we apply a time-varying excitation field, the FFP is shifted rapidly across the field-of-view (FOV). The SPIOs lying within the FFP respond to this rapid change in magnetic field by flipping their magnetization 180°, whereas the particles elsewhere remain saturated. Since the receiver coil detects time-varying magnetizations, only the SPIOs at the FFP produce an MPI signal. Because the tissue is transparent to the excitation field, we only detect the SPIO nanoparticles injected into the body, with no signal from tissue. The resulting *positive* contrast from the SPIOs is linear, sensitive, and repeatable, which makes MPI's contrast comparable to that seen in nuclear imaging.

The first technique developed for image reconstruction in MPI was *system function* reconstruction [1, 26, 30, 31]. S*ystem function* reconstruction relies on pre-characterization

of the system matrix followed by matrix inversion. The pre-characterization step involves estimating a *system matrix* by measuring the signal response from a point source of particles at every possible location in the imaging FOV. These measurements can be time consuming, scaling with the size of the FOV and the desired resolution. Another possible concern is that the *system matrix* is usually acquired in water, which has a different viscosity than blood [32]. Hence, the pre-characterization may not accurately reflect the microenvironment *in vivo*. In addition, the matrix inversion process may be computationally intense, and if deconvolution is employed, it may amplify noise by the condition number of the system matrix [33]. A comprehensive discussion of the system function and its key properties can be found in [26, 30]. To improve the speed and robustness of image reconstruction in MPI, we have recently introduced the X-space reconstruction [22, 27], which we describe in detail next.

X-Space MPI

The basic signal equation of any imaging technique reveals the resolution and reconstruction fundamentals of that technique. For example, MRI researchers rely extensively on *k*-space analysis [2, 3] to craft efficient pulse sequences and to predict fundamental metrics of the MRI scan, including sensitivity, contrast, aliasing and spatial resolution. The *k*-space theory also reliably predicts the appearance of artifacts from motion, aliasing, and B_0 distortion.

With strong parallels to *k*-space in MRI, we recently introduced the x-space reconstruction technique [22, 27] to improve both the robustness and the speed of MPI image reconstructions. The key difference is that the MPI signal represents a temporal scan through the spatial image domain, or *x-space,* instead of a temporal scan through the spatial-frequency domain, or *k*-space, in MRI. The raw MPI signal is converted into an x-space MPI image using a very fast and robust two-step process of velocity compensation followed by gridding to the instantaneous position of the FFP. No matrix inversion or pre-characterization is required, and no modeling regarding the *in vivo* microenvironment is needed; hence, the x-space image reconstruction algorithm is robust and real-time.

Let us compare *k*-space analysis and x-space analysis through their basic signal equations. The MRI signal equation using the *k*-space formulation is:

$$s(t)=\rho(k(t)), \text{ where } k(t)=\frac{\gamma}{2\pi}\int_0^t g(r)dr \quad (1)$$

where is ρ(k) the Fourier transform of the proton distribution, ρ(x), and k(t) is the instantaneous *k*-space position that is being sampled, which is the integral of the time-varying magnetic field gradients, g(t), multiplied by the gyromagnetic ratio.

In a similar manner, we can describe MPI using x-space analysis. The MPI signal equation (omitting constant multipliers for simplicity) has a similar form:

$$s(t)=\beta(x_2(t))x_2(t) \quad (2)$$

where β(x) is the "native" MPI image of nanoparticle distribution, $x_2(t)$ is the instantaneous position of the FFP, and $x_2(t)$ is the instantaneous velocity of the FFP. Here we define *native MPI image* as the nanoparticle density convolved with the point spread function (PSF) of the system.

$$\beta(x)=h(x)*\rho(x) \quad (3)$$

where we and others [26] have found both experimentally and theoretically [22] that the 1D PSF is:

$$h(x)=L\left(\frac{Gx}{H_{\text{sat}}}\right)=\frac{1}{\left(\frac{Gx}{H_{\text{sat}}}\right)^2}-\frac{1}{sinh^2\left(\frac{Gx}{H_{\text{sat}}}\right)} \quad (4)$$

with L(·) defined as the derivative of the Langevin function that characterizes SPIO magnetization. This PSF is similar in shape to a Lorentzian function (see Fig. 2a). Here, G [T/m/ $_0$] is the gradient strength and H_{sat} [A/m] is the field required to half saturate the SPIOs. Readers should note that the MPI notation has evolved to specify magnetic fields in A/m rather than adopting the MRI tradition of specifying the induction fields in Tesla; although practically the two fields are interchangeable since the diamagnetic values of tissue ($\chi \approx -9 \times 10^{-6}$) are so small that susceptibility effects (e.g., lung air-tissue interface) have completely negligible effect in MPI scans. Indeed, magnetic field distortions of even a few percent cause negligible image artifacts in MPI, whereas implanted metal (e.g., cobalt chrome, stainless steel, and titanium with non-magnetic susceptibilities $|\chi| < 1 \times 10^{-3}$ [28]) is well-known to produce complete T2* dropouts in MRI. Hence, MPI is dramatically more robust to field distortions than MRI.

In x-space image reconstruction, we convert the raw MPI signal, s(t), into the reconstructed MPI image, β(x), using a fast and robust gridding operation. This gridding requires only the knowledge of the instantaneous FFP position and the FFP velocity through space, both of which are controlled by the user-defined imaging *pulse sequence*. To form an image, we normalize the received MPI signal by the FFP velocity and grid to the instantaneous location of FFP (see Fig. 2c), i.e.,

$$IMG(x_2(t))=\beta(x_2(t))=\frac{s(t)}{x_2(t)} \quad (5)$$

Note that this simple reconstruction process does not require any *a priori* knowledge of the 1D PSF given in Eq. 4. The technique reconstructs a native undeconvolved MPI image, whose resolution is defined only by the strength of the agnetic field gradient and the magnetic properties of the nanoparticle tracer. Some of the key implications of spatial x-space scanning in MPI as opposed to *k*-space scanning in MRI are listed in Table 1.

As seen in the above-given relations, the MPI signal is linear with nanoparticle density. In fact, as shown in Fig. 3a, our experimental results validate that MPI's positive contrast signal is perfectly linear ($R^2 = 0.99$) with input nanoparticle quantity. The full-width-at-half-maximum (FWHM) of the PSF tells us that the resolution improves linearly with gradient strength, and *cubically* with magnetic nanoparticle diameter [22, 26], i.e.,

$$\Delta x=\frac{24k_BT}{\mu_0\pi M_{\text{sat}}Gd^2} \quad (6)$$

where d [m] is the magnetic core diameter, M_{sat} [A/m] is the saturation magnetization of the SPIOs, T is temperature, μ_0 is the vacuum permeability, and k_B is Boltzmann's constant. This dependence on gradient strength and particle diameter is illustrated in Fig. 3b, where the resolution of our two MPI scanners in Fig. 1 are marked for a 20 nm magnetic core size (similar to the effective magnetic size of Resovist SPIOs). When it comes to tracer sensitivity and resolution, MPI already performs well in comparison with other small animal (pre-clinical) imaging modalities (see Fig. 3b,c). With imaging/hardware improvements and development of tailored nanoparticles, we expect MPI to achieve sub-mm resolutions with micromolar level sensitivity within the next couple of years.

Although the resolution is expected to improve cubically with the magnetic core size, increasing particle sizes leads to increasing nanoparticle relaxation effects. Relaxation affects the resulting MPI images because it prevents the SPIO magnetization from instantaneously rotating to follow FFP (see Fig. 4). As demonstrated in Fig. 4a, this delay is caused by forces such as thermal motion and viscous friction, which act against the particle's alignment with the applied field. These relaxation delays are also dependent on SPIO characteristics, such as the hydrodynamic volume of the particle, and cause blurring in the image [34–36]. Relaxation effects can be difficult to distinguish from hysteresis effects, which we might expect to see for multi-domain particles. In either case, optimal SPIO synthesis is essential to achieve spatial resolutions that are competitive with MRI or CT. Developing new SPIOs that are tailored specifically for MPI has become a burgeoning area of research [34, 37]. Figure 4b shows TEM images of tailored nanoparticles with 20 nm mean iron oxide core diameter, in comparison with a commercially available contrast agent, Resovist. These tailored nanoparticles, synthesized in University of Washington, already perform better than Resovist with their comparable resolution (see Fig. 4c) and improved signal levels.

3. MPI Hardware

There are two main classes of MPI imagers: Field Free Point (FFP) and Field Free Line (FFL) imagers. The main difference between these two classes is the design of the main magnetic field gradient, or selection field. The vast majority of MPI scanners use a strong, static field gradient to produce a FFP, which is the location where the magnetic field magnitude is weaker than the saturation magnetization of a magnetic nanoparticle tracer. An image is formed by scanning the FFP across an FOV.

We typically implement scanning with a combination of slow, high-strength magnets and fast, low-strength magnets. This approach allows us to scan with good sensitivity while staying within human safety thresholds. To image a bigger FOV than the one covered by the rapid excitation field, we can also shift the FFP mechanically and/or electronically [38–41]. Electronic shifting is done by adding a uniform magnetic field with amplitude that varies slowly in time.

Recently, an MPI scanner featuring two-dimensional projection mode was demonstrated [25]. A projection MPI scanner requires a strong selection field that creates a zero field along a line, and this has been termed a field free line (FFL) magnet [42–47]. These FFL MPI scanners effectively acquire the integral of the nanoparticle signal along the FFL, producing 2D projection images that are conceptually similar to those produced by X-ray and X-ray fluoroscopic imaging. Projection imaging has many benefits, most notably higher imaging speed or higher SNR [25].

By rotating and translating the location of the projection FFL direction, we can create an MPI dataset that can be reconstructed via standard CT methods (e.g., filtered backprojection) to form a three-dimensional MPI image with nearly 10-fold SNR improvement [48], as shown in Figs. 7 and 8. Other FFL MPI magnet designs and reconstruction techniques have been proposed, but not yet demonstrated [42–47].

One important implementation detail for all MPI scanners is suppressing direct feedthrough. In NMR and MRI, thanks to the relatively slow T_2 relaxation, we typically can separate transmit and receive by several milliseconds. Therefore, direct feedthrough of the (much larger) transmit field is not a challenge. In MPI, the SPIO nanoparticles respond almost instantaneously to the applied field, requiring simultaneous transmit/receive. Hence, direct feedthrough is always a serious challenge [41, 49]. We must filter out the scanning

frequency not only by geometrical decoupling of transmit and receive, but also with high-order notch filters and/or high-pass filters in frequency domain.

Shown in Fig 1 are FFP and FFL imagers built at UC Berkeley. The FFP imager (Fig. 1a,b) is constructed using opposed NdFeB permanent magnet cylinders that produce a strong gradient of 7 T/m in the x axis, and 3.5 T/m in the y and z axes [50]. The asymmetry of gradient strengths in the three axes is an unavoidable requirement of Maxwell's equations [27]. The system is water-cooled and consumes approximately 30 kW continuously during imaging. Images produced by the system have ~2 millimeter resolution using Resovist tracer, and an example image can be seen in Fig. 1c. The FFL projection imager (Fig. 1d,e) is constructed using two rectangular NdFeB permanent magnet subassemblies that produce a 2.4 T/m magnetic field gradient in the x and z axes. The remaining instrument axis, the y axis, has a significantly weaker gradient field strength of 0.08 T/m and corresponds to the "Field Free Line (FFL)" direction. The FFL produces projection MPI images such as the one shown in Fig. 1f. As expected, the FFL imager has approximately three times lower resolution than the FFP imager solely due to the weaker magnetic gradient strength (i.e., 2.4 T/m vs. 7 T/m).

In addition to FFP and projection (FFL) MPI, we also constructed a third class of MPI imager called a "narrowband" MPI imager [51]. The narrowband MPI method uses an inter-modulation excitation followed by a narrowband receiver coil. This method may offer improved SNR due to significantly better noise matching over the narrow bandwidth of the receive coil.

4. Current Biomedical Applications of MPI

MPI has great potential to revolutionize angiography and stem cell imaging. Here we illustrate these two biomedical applications with our latest data.

Safe Angiography

MPI offers great hope to increase angiographic imaging safety and efficacy for CKD patients. Three kidney-safe SPIO contrast agents (AMI-121, OMP, and AMI-25) are already approved for human clinical studies [52]. There is ample evidence in the literature that patients with CKD will tolerate SPIO contrast agents far better than iodine or gadolinium [53]. Furthermore, MPI has no depth attenuation, no background tissue signal, and is perfectly linear, which are key characteristics for an angiographic imaging modality.

MPI's near-perfect signal linearity allows the detection of arterial narrowings, even for arteries that are smaller than the MPI system resolution. Narrowed arteries will have a proportionally smaller tracer content than healthy arteries, which will allow detection in an MPI Scanner. Figure 5 illustrates this concept. The narrowing of an "artery" is demonstrated in an acrylic phantom, and remains visible despite showing occlusion that nears the resolution limit of the system. Similarly, Fig. 6 demonstrates both the high contrast and high-resolution capabilities of MPI. Here, an *ex vivo* rabbit kidney was injected with 3× diluted Resovist tracer into ureter, and washed with DI water. The MPI images show the Resovist in the ureter and the renal pelvis right after the initial injection, and entering the renal medulla after the washing with DI water.

MPI has the ideal contrast for angiography. No signal is produced by tissue; thus the artifacts often seen by ribs or other bodily structures seen in X-ray and CTA are not present in MPI. Figure 7 shows a post-mortem MPI image of a mouse injected with 100 L undiluted Resovist via the tail vein and sacrificed 30 s post-injection. The mouse was imaged using Projection Reconstruction MPI and the resulting dataset was volume rendered. The MPI

image shows the Resovist in the heart and filtering in the liver. Note the millimeter-scale resolution of the system, and that there is no signal from the mouse tissue.

To further verify that the tissue does not generate any signal or cause depth attenuation of the MPI signal, a phantom without and with tissue was imaged. As shown in Fig. 8, a helical phantom was created by winding 0.8 mm inner diameter tubing around a section of 2.6 cm outer diameter acrylic tubing, and 10× diluted (50 mM) Resovist was injected into the tubing. The phantom was then imaged with a full Projection Reconstruction (PR) imaging protocol using the projection MPI scanner and a rotary sample stage. The resulting three-dimensional projection-reconstructed image was then maximum intensity projected. The phantom was subsequently covered with tissue (*Meleagris Gallopavo*) and imaged a second time. The resulting images are shown in Fig. 8a,b. No further image processing (i.e., no non-linear windowing, offsetting, or deconvolution) was performed on the images. When we compare the images with and without tissue, we saw only a negligible difference in raw signals, which can be explained by differences in transmit coil loading from the tissue. Hence, we conclude that tissue has no MPI signal and does not cause any depth attenuation of the MPI signal. These features of MPI make it an ideal imaging method for high-contrast, high-sensitivity angiography.

Stem Cell Tracking

Additionally, MPI has extraordinary potential for imaging and tracking stem cells in cell therapy applications. Stem cell therapy has great promise for healing damaged organs, including spinal cord injuries [54], diabetic pancreatic cells [55], infarcted myocardium [56], and dopamine neurons in Parkinson's disease [57], yet no satisfactory *in vivo* imaging method currently exists to confirm the accuracy of stem cell targeting and long-term cell viability in these organs. Comparing existing imaging modalities (i.e., PET, SPECT, X-ray, bioluminescence, NIR fluorescence, ultrasound, and MRI) for tracking stem cells *in vivo*, Frangioni and Hajjar concluded that "…*no currently available imaging technology is ideal*" [58]. They are limited in contrast sensitivity, resolution, and/or quantification. For example, due to its depth attenuation, bioluminescence is applicable to only small animal studies, and cannot be successfully translated to humans. In contrast, MPI is well suited for stem cell imaging because it produces images with extremely high contrast, zero depth attenuation of signal, high sensitivity, and the ability to accurately quantify cell number *in vivo*.

In Fig. 9, we demonstrate MPI for stem cell tracking. Here, human embryonic stem cell (hESC)-derived cells were labeled with Resovist SPIOs [59] and injected subdermally into a postmortem mouse in two injections. Figure 9a shows a projection MPI image of the mouse, taken on the UC Berkeley projection MPI scanner, followed by a mild Wiener deconvolution. As in MRI, the MPI image shows no depth attenuation. Additionally, no background signal from the mouse tissue is present in the image, showing that MPI can have extremely high contrast and sensitivity.

In addition to providing excellent contrast and tissue transparency, MPI is also able to quantify stem cells in the imaging volume. Taking Fig. 9a as an example, roughly twice the number of cells were injected in the right injection than in the left. In the MPI image, the ratio of the signal intensities between the right and left injection sites was also found to be 2.1. Another example is shown in Fig. 9b, where a series of labeled hESC-derived cells were imaged in the projection scanner. When the maximum signal intensity from each scan was plotted against the number of scanned cells, an excellent linear fit was found ($R^2 = 0.99$). The current stem cell detection threshold is limited by system interference [49] and is approximately 1×10^4 cells in our prototype system. However, there remains significant room for improvement, and the theoretical detection threshold in the UC Berkeley projection scanner is as little as 500 cells, with potential for orders-of-magnitude improvement through

optimal receive coils, preamplifiers, and nanoparticles. With further advances in scanner technology and nanoparticle science, dedicated MPI scanners show tremendous potential for sensitive, quantitative, and high-contrast imaging of stem cell therapies for research and clinical purposes.

5. Future Directions for MPI

In addition to angiography and stem cell tracking, MPI offers an exciting array of potential applications such as real-time fluoroscopy, diagnosis and staging of cancer, *in vivo* inflammation imaging, and temperature mapping [60]. Furthermore, MPI shows promise as a "functional" molecular imaging method through improved chemistry on the SPIO nanoparticle coating. This might include binding to chemicals that can alter the speed at which the SPIOs align with the applied field, creating a new type of biochemical contrast mechanism. In the following sections, we discuss some of these future directions for MPI, including construction of human-size MPI scanners.

MPI Fluoroscopy

Fast and strong gradients, parallel imaging methods, and compressed sensing techniques have all pushed MRI to clinically relevant real-time sequences. Yet despite these advances, X-ray angiography and X-ray fluoroscopic interventional imaging are still the industry standards after ~50 years.

A key attribute of an X-ray fluoroscopy system is the real-time, interactive 15 to 30 fps frame-rate at full-resolution. To compete, MPI must achieve both real-time acquisition and reconstruction at interactive speeds. Amazingly, MPI images at 47 fps acquisition (21.5 ms temporal resolution) with off-line reconstruction have already been demonstrated across a small 3D FOV using a system function approach [31].

Our work on projection MPI (See Fig. 1) using a Field Free Line is a first step to achieving real-time MPI across clinically relevant FOVs, such as the heart or the brain. The key enabling feature of projection MPI is a dramatically reduced scan time compared to 3D imaging [25]. 2D projection imaging coupled with computationally efficient and straightforward x-space reconstruction could enable MPI "fluoroscopy" for both diagnostic and interventional MPI. Because of the speed and/or SNR benefits, we believe projection imaging may one day be the preferred mode of use for the MPI technique.

Functional and "Smart" Nanoparticles

The ability of the MPI technique to sensitively detect untagged and targeted magnetic nanoparticle tracers may enable new approaches to cancer diagnosis and staging, atherosclerotic plaque detection, inflammation imaging, and relaxation contrast.

MRI and CT typically detect cancer through an untagged functional imaging approach that highlights areas of enhanced permeability and retention (EPR) using gadolinium or iodine [61]. The same procedure can be performed using SPIO nanoparticles [62] and MPI. Since it is crucial for staging to establish whether a tumor has expanded beyond an organ boundary, we expect that an anatomic reference scan taken with CT or MRI will be important, much like PET/CT. Note that this anatomic reference is not needed for angiograms, MPI or otherwise.

It is also possible to functionalize SPIO nanoparticles using peptides or antibodies. Functionalized nanoparticles then would adhere to a biological target, such as tumor cells or atherosclerotic plaque. The SPIOs can still be detected magnetically after the surface is modified for targeting. For example, SPIOs functionalized with the CREKA peptide have

been shown to bind to clots present both at plaque formation and tumor sites [63, 64], and SPIOs with variants of a RGD peptide target a specific integrin present at both atherosclerotic plaques and on tumor cells [65, 66].

MPI may also be able to track and quantitate inflammation. Inflammation can be targeted by tailoring SPIOs to be uptaken by immune cells using standard dextran coatings [67, 68]. To tag immune cells, we simply inject the coated particles and exploit the RES system to scavenge the particles. Sites of ongoing inflammation immediately uptake the tracer, such as phagocytic inflammatory cells at sites of tumors [69, 70] and atherosclerotic plaques [71, 72]. A scan taken several hours later may reveal other sites of inflammation that are subsequently targeted by other SPIO-tagged immune cells. Other studies suggest that smart targeting agents [63] could offer significant improvement in the specificity of inflammation imaging.

We may also be able to produce functional information in an MPI image that shows nanoparticle binding state and the viscosity of the microenvironment using *relaxation contrast* imaging. The relaxation state of a nanoparticle ensemble can be measured using a specially designed pulse sequence. The change in relaxation characteristics of functionalized SPIOs following binding to their targets has been demonstrated [73, 74] in non-imaging systems [75], and it remains to be demonstrated in a tomographic MPI imager. Similarly, a change in temperature can also alter the relaxation contrast, which can be exploited for temperature mapping with MPI [60].

Human-Size MPI Scanners

In an analogous fashion to MRI, MPI can be scaled up to human sizes from pre-clinical mouse-sized imagers such as the systems shown in this paper. Significant work remains until MPI can become clinically relevant, particularly with regards to building new generations of MPI scanning hardware and developing new scanning methodologies. Fortunately, we see no fundamental hardware or physics limitation that would prevent scaling MPI up to human sizes. A human MPI scanner would require a much heavier permanent magnet gradient, yoked electromagnet gradient, or perhaps a superconducting gradient. A superconducting gradient would put system costs and complexity similar to that of a modern 1.5 T superconducting MRI scanner. The human-bore field gradient is certainly feasible; for example, a commercially available 3T MRI scanner has a 7.2 T/m maximum spatial gradient just outside its bore [76]. With no deconvolution and using Resovist (rather than an MPI-tailored SPIO agent) we could expect 1.5 mm resolution at that gradient strength, which is already clinically relevant. Moreover, MPI-tailored SPIOs could *significantly* improve this spatial resolution. Numerous groups are developing some of the first pre-clinical imagers but there exists, at present, no commercially available scanner.

In addition to scaling up the hardware, understanding the safety limits of the applied magnetic fields will be critical during translation to human-size MPI scanners. The strong static gradient field in MPI creates the risk of ferromagnetic objects being pulled into the scanner [77]. This safety risk is very similar to the well-established risk from the B_0 field gradients outside the bore of an MRI scanner. Hence, MPI's static gradient field is subject to the same precautions as the B_0 field in MRI: patients and potentially ferromagnetic objects need to be screened carefully. The time-varying excitation field in MPI, on the other hand, is subject to magnetostimulation and SAR limits, just like the gradient and RF fields of MRI. Most MPI scanners today use an excitation field in the 5–25 kHz range [1, 22, 25, 27, 78]. Shown in Fig. 10 are the magnetostimulation and SAR limits in and around this frequency range. In this figure, the magnetostimulation thresholds were extrapolated using the human-subject experiments in the arm and leg given in Fig. 10.b,c [79] and assuming a radius of r = 20 cm (typical radius of human torso). The SAR threshold curve was calculated for a

continuous (i.e., 100% duty cycle) sinusoidal magnetic field and a 4 W/kg limit [80]. To avoid safety hazards, we need to operate below both the magnetostimulation and SAR limit curves at all times. Therefore, for the 5–25 kHz range excitation field in MPI, magnetostimulation is the primary safety concern. Further research on safety limits, especially on magnetostimulation at higher frequencies [81] or human-subject experiments on the torso, are needed for more accurate determination of the safety limits for a human-size MPI scanner. We believe that, just as in the MRI case, fast MPI methods that adhere to dB/dt limits will be an exciting future area of research.

6. Conclusion

The development of Magnetic Particle Imaging is just beginning and in many ways parallels the development of MRI in the early 1980s. The technical background in NMR/MRI makes accessible some of the key hardware and theoretical components of MPI, including magnetic field gradients, low noise receive coils and pre-amplifiers, and image reconstruction methods. In particular, we believe that the parallels between *k*-space in MRI and x-space in MPI will be readily apparent to seasoned NMR/MRI researchers and will spur innovations in pulse sequence design and image reconstruction, just as in MRI.

In pre-clinical imaging, MPI shows great promise for biomedical imaging applications such as angiography, dynamic contrast enhancement, cell tracking, inflammation imaging, and targeted nanoparticle imaging due to the relative ease at which SPIO nanoparticles can be injected, attached to cells, or conjugated to peptides. These prospective applications are still early in their development cycle and could have substantial diagnostic utility. Our initial results for angiography and cell tracking shown in this paper detail the excellent sensitivity and near perfect contrast inherent to the technique, but both engineering and biological work remains until the technique can compare with the spatial resolution seen in modern MRI.

The earliest clinical applications of MPI may be motivated by the extraordinary safety of SPIO tracers in Chronic Kidney Disease patients. Before MPI systems can make their way to the clinics, of course, there are several engineering hurdles including building human-sized MPI scanners. Fortunately, we see no fundamental limits to scaling MPI to human sizes, and so the future looks bright for MPI.

Acknowledgments

EU Saritas and PW Goodwill contributed equally to this work. This work was supported in part by CIRM Tools and Technology Grant RT2-01893, National Institute of Biomedical Imaging and Bioengineering Grant Number 1R01EB013689, and a UC Discovery grant. The contents of this publication are solely the responsibility of the authors and do not necessarily represent the official views of CIRM, the National Institute of Biomedical Imaging and Bioengineering, the National Institutes of Health, or any other agency of the State of California.

References

1. Gleich B, Weizenecker R. Tomographic imaging using the nonlinear response of magnetic particles. Nature. 2005; 435:1214–1217. [PubMed: 15988521]
2. Ljunggren S. A Simple Graphical Representation of Fourier-Based Imaging Methods. J Magn Reson. 1983; 54:338–343.
3. Twieg DB. The K-Trajectory Formulation of the Nmr Imaging Process with Applications in Analysis and Synthesis of Imaging Methods. Med Phys. 1983; 10:610–621. [PubMed: 6646065]
4. Jiaquan Xu KDK, Murphy Sherry L, Tejada-Vera Betzaida. Deaths: Final Data for 2007, CDC: National Vital Statistics Reports. 2010; 58
5. Katzberg RW, Haller C. Contrast-induced nephrotoxicity: clinical landscape. Kidney Int Suppl. 2006:S3–S7. [PubMed: 16612398]

6. Rudnick MR, Goldfarb S, Tumlint J. Contrast-induced nephropathy: Is the picture any clearer? Clin J Am Soc Nephro. 2008; 3:261–262.
7. Reddan DN, Szczech LA, Tuttle RH, Shaw LK, Jones RH, Schwab SJ, Smith MS, Califf RM, Mark DB, Owen WF. Chronic kidney disease, mortality, and treatment strategies among patients with clinically significant coronary artery disease. J Am Soc Nephrol. 2003; 14:2373–2380. [PubMed: 12937316]
8. Ix JH, Mercado N, Shlipak MG, Lemos PA, Boersma E, Lindeboom W, O'Neill WW, Wijns W, Serruys PW. Association of chronic kidney disease with clinical outcomes after coronary revascularization: The arterial revascularization therapies study (ARTS). Am Heart J. 2005; 149:512–519. [PubMed: 15864241]
9. Goldfarb S, McCullough PA, McDermott J, Gay SB. Contrast-Induced Acute Kidney Injury: Specialty-Specific Protocols for Interventional Radiology, Diagnostic Computed Tomography Radiology, and Interventional Cardiology. Mayo Clin Proc. 2009; 84:170–179. [PubMed: 19181651]
10. McCullough P. Outcomes of contrast-induced nephropathy: Experience in patients undergoing cardiovascular intervention. Catheter Cardio Inte. 2006; 67:335–343.
11. McCullough PA. Contrast-induced acute kidney injury. J Am Coll Cardiol. 2008; 51:1419–1428. [PubMed: 18402894]
12. Broome DR. Nephrogenic systemic fibrosis associated with gadolinium based contrast agents: A summary of the medical literature reporting. Eur J Radiol. 2008; 66:230–234. [PubMed: 18372138]
13. Collidge TA, Thomson PC, Mark PB, Traynor JP, Jardine AG, Morris STW, Simpson K, Roditi GH. Gadolinium-enhanced MR imaging and nephrogenic systemic fibrosis: Retrospective study of a renal replacement therapy cohort. Radiology. 2007; 245:168–175. [PubMed: 17704357]
14. Sadowski EA, Bennett LK, Chan MR, Wentland AL, Garrett AL, Garrett RW, Djamali A. Nephrogenic systemic fibrosis: Risk factors and incidence estimation. Radiology. 2007; 243:148–157. [PubMed: 17267695]
15. Nishimura DG, Macovski A, Pauly JM, Conolly SM. Mr Angiography by Selective Inversion Recovery. Magn Reson Med. 1987; 4:193–202. [PubMed: 3561250]
16. Brittain JH, Olcott EW, Szuba A, Gold GE, Wright GA, Irarrazaval P, Nishimura DG. Three-dimensional flow-independent peripheral angiography. Magn Reson Med. 1997; 38:343–354. [PubMed: 9339435]
17. Miyazaki M, Sugiura S, Tateishi F, Wada H, Kassai Y, Abe H. Non-contrastenhanced MR angiography using 3D ECG-synchronized half-Fourier fast spin echo. J Magn Reson Imaging. 2000; 12:776–783. [PubMed: 11050650]
18. Dias MHM, Lauterbur PC. Ferromagnetic Particles as Contrast Agents for Magnetic-Resonance-Imaging of Liver and Spleen. Magn Reson Med. 1986; 3:328–330. [PubMed: 3713497]
19. Weissleder R, Stark DD, Engelstad BL, Bacon BR, Compton CC, White DL, Jacobs P, Lewis J. Superparamagnetic Iron-Oxide - Pharmacokinetics and Toxicity. Am J Roentgenol. 1989; 152:167–173. [PubMed: 2783272]
20. Ferrucci JT, Stark DD. Iron-Oxide Enhanced Mr-Imaging of the Liver and Spleen - Review of the 1st-5 Years. Am J Roentgenol. 1990; 155:943–950. [PubMed: 2120963]
21. Lu M, Cohen MH, Rieves D, Pazdur R. FDA report: Ferumoxytol for intravenous iron therapy in adult patients with chronic kidney disease. Am J Hematol. 2010; 85:315–319. [PubMed: 20201089]
22. Goodwill PW, Conolly SM. The X-Space Formulation of the Magnetic Particle Imaging Process: 1-D Signal, Resolution, Bandwidth, SNR, SAR, and Magnetostimulation. IEEE T Med Imaging. 2010; 29:1851–1859.
23. Goodwill PW, Saritas EU, Croft LR, Kim TN, Krishnan KM, Schaffer DV, Conolly SM. X-Space MPI: Magnetic Nanoparticles for Safe Medical Imaging. Adv Mater. 2012; 24:3870–3877. [PubMed: 22988557]
24. Goodwill PW, Tamrazian A, Croft LR, Lu CD, Johnson EM, Pidaparthi R, Ferguson RM, Khandhar AP, Krishnan KM, Conolly SM. Ferrohydrodynamic relaxometry for magnetic particle imaging. Appl Phys Lett. 2011; 98

25. Goodwill PW, Konkle JJ, Zheng B, Saritas EU, Conolly SM. Projection X-Space Magnetic Particle Imaging. IEEE T Med Imaging. 2012; 31:1076–1085.
26. Rahmer J, Weizenecker J, Gleich B, Borgert J. Signal encoding in magnetic particle imaging: properties of the system function. BMC Med Imaging. 2009; 9:4. [PubMed: 19335923]
27. Goodwill PW, Conolly SM. Multidimensional X-Space Magnetic Particle Imaging. IEEE T Med Imaging. 2011; 30:1581–1590.
28. Schenck JF. The role of magnetic susceptibility in magnetic resonance imaging: MRI magnetic compatibility of the first and second kinds. Med Phys. 1996; 23:815–850. [PubMed: 8798169]
29. Rosensweig, RE. Ferrohydrodynamics. Cambridge ; New York: Cambridge University Press; 1985.
30. Rahmer J, Weizenecker J, Gleich B, Borgert J. Analysis of a 3-D System Function Measured for Magnetic Particle Imaging. IEEE T Med Imaging. 2012; 31:1289–1299.
31. Weizenecker J, Gleich B, Rahmer J, Dahnke H, Borgert J. Three-dimensional real-time in vivo magnetic particle imaging. Phys Med Biol. 2009; 54:L1–L10. [PubMed: 19204385]
32. Fahraeus R, Lindqvist T. The viscosity of the blood in narrow capillary tubes. Am J Physiol. 1931; 96:562–568.
33. Knopp T, Biederer S, Sattel TF, Erbe M, Buzug TM. Prediction of the Spatial Resolution of Magnetic Particle Imaging Using the Modulation Transfer Function of the Imaging Process. IEEE T Med Imaging. 2011; 30:1284–1292.
34. Ferguson RM, Minard KR, Krishnan KM. Optimization of nanoparticle core size for magnetic particle imaging. J Magn Magn Mater. 2009; 321:1548–1551. [PubMed: 19606261]
35. Croft LR, Goodwill PW, Conolly SM. Relaxation in X-Space Magnetic Particle Imaging. IEEE T Med Imaging. 2012 Accepted.
36. Croft, LR.; Goodwill, P.; Ferguson, M.; Krishnan, K.; Conolly, S. Relaxation in x-space Magnetic Particle Imaging. In: Borgert, TMBaJ, editor. Magnetic Particle Imaging. Lubeck, Germany: Springer Proceedings in Physics; 2012. p. 149-153.
37. Ferguson RM, Minard KR, Khandhar AP, Krishnan KM. Optimizing magnetite nanoparticles for mass sensitivity in magnetic particle imaging. Med Phys. 2011; 38:1619–1626. [PubMed: 21520874]
38. Gleich, B.; Weizenecker, J.; Timminger, H.; Bontus, C.; Schmale, I.; Rahmer, J.; Schmidt, J.; Kanzenbach, j; Borgert, J. Fast MPI demonstrator with enlarged field of view; 18th Annual Meeting of ISMRM, Stockholm, Sweden; 2010. p. 218
39. Rahmer, J.; Gleich, B.; Bontus, C.; Schmale, I.; Schmidt, J.; Kanzenbach, J.; Woywode, O.; Weizenecker, J.; Borgert, J. Results on rapid 3D magnetic particle imaging with a large field of view; 19th Annual Meeting of ISMRM, Montreal, Canada; 2011. p. 629
40. Goodwill PW, Lu K, Zheng B, Conolly SM. An x-space magnetic particle imaging scanner. Rev Sci Instrum. 2012; 83
41. Lu, K.; Goodwill, P.; Conolly, S. Linear and Shift Invariance of Magnetic Particle Imaging. In: Borgert, TMBaJ, editor. Magnetic Particle Imaging. Lubeck, Germany: Springer Proceedings in Physics; 2012. p. 155
42. Weizenecker J, Gleich B, Borgert J. Magnetic particle imaging using a field free line. J Phys D Appl Phys. 2008; 41
43. Knopp T, Erbe M, Sattel TF, Biederer S, Buzug TM. A Fourier slice theorem for magnetic particle imaging using a field-free line. Inverse Probl. 2011; 27
44. Erbe M, Knopp T, Sattel TF, Biederer S, Buzug TM. Experimental generation of an arbitrarily rotated field-free line for the use in magnetic particle imaging. Med Phys. 2011; 38:5200–5207. [PubMed: 21978064]
45. Knopp T, Sattel TF, Biederer S, Buzug TM. Field-free line formation in a magnetic field. J Phys a-Math Theor. 2010; 43
46. Knopp T, Erbe M, Biederer S, Sattel TF, Buzug TM. Efficient generation of a magnetic field-free line. Med Phys. 2010; 37:3538–3540. [PubMed: 20831060]
47. Knopp T, Erbe M, Sattel TF, Biederer S, Buzug TM. Generation of a static magnetic field-free line using two Maxwell coil pairs. Appl Phys Lett. 2010; 97

48. Konkle, J.; Goodwill, P.; Carrasco-Zevallos, O.; Conolly, S. Experimental 3D X-Space Magnetic Particle Imaging Using Projection Reconstruction. In: Borgert, TMBaJ, editor. Magnetic Particle Imaging. Lubeck, Germany: Springer Proceedings in Physics; 2012. p. 243-247.
49. Zheng, B.; Goodwill, P.; Yang, W.; Conolly, S. Capacitor Distortion in Magnetic Particle Imaging. In: Borgert, TMBaJ, editor. Magnetic Particle Imaging. Springer Proceedings in Physics; Lubeck, Germany: 2012. p. 319-324.
50. Goodwill, P.; Croft, L.; Konkle, J.; Lu, K.; Saritas, E.; Zheng, B.; Conolly, S. Borgert, TMB.a.J Magnetic Particle Imaging. Lubeck, Germany: Springer Proceedings in Physics; 2012. Third Generation X-space MPI Mouse and Rat Scanner; p. 261-265.
51. Goodwill PW, Scott GC, Stang PP, Conolly SM. Narrowband magnetic particle imaging. IEEE T Med Imaging. 2009; 28:1231–1237.
52. LaConte L, Nitin N, Bao G. Magnetic nanoparticle probes. Materials Today. 2005; 8:32–38.
53. Neuwelt EA, Hamilton BE, Varallyay CG, Rooney WR, Edelman RD, Jacobs PM, Watnick SG. Ultrasmall superparamagnetic iron oxides (USPIOs): a future alternative magnetic resonance (MR) contrast agent for patients at risk for nephrogenic systemic fibrosis (NSF)? Kidney Int. 2009; 75:465–474. [PubMed: 18843256]
54. Kim SU, de Vellis J. Stem Cell-Based Cell Therapy in Neurological Diseases: A Review. J Neurosci Res. 2009; 87:2183–2200. [PubMed: 19301431]
55. Hess D, Li L, Martin M, Sakano S, Hill D, Strutt B, Thyssen S, Gray DA, Bhatia M. Bone marrow-derived stem cells initiate pancreatic regeneration. Nat Biotechnol. 2003; 21:763–770. [PubMed: 12819790]
56. Jackson KA, Majka SM, Wang HG, Pocius J, Hartley CJ, Majesky MW, Entman ML, Michael LH, Hirschi KK, Goodell MA. Regeneration of ischemic cardiac muscle and vascular endothelium by adult stem cells. J Clin Invest. 2001; 107:1395–1402. [PubMed: 11390421]
57. Kim JH, Auerbach JM, Rodriguez-Gomez JA, Velasco I, Gavin D, Lumelsky N, Lee SH, Nguyen J, Sanchez-Pernaute R, Bankiewicz K, McKay R. Dopamine neurons derived from embryonic stem cells function in an animal model of Parkinson's disease. Nature. 2002; 418:50–56. [PubMed: 12077607]
58. Frangioni JV, Hajjar RJ. In vivo tracking of stem cells for clinical trials in cardiovascular disease. Circulation. 2004; 110:3378–3383. [PubMed: 15557385]
59. Arbab AS, Yocum GT, Kalish H, Jordan EK, Anderson SA, Khakoo AY, Read EJ, Frank JA. Efficient magnetic cell labeling with protamine sulfate complexed to ferumoxides for cellular MRI. Blood. 2004; 104:1217–1223. [PubMed: 15100158]
60. Weaver JB, Rauwerdink AM, Hansen EW. Magnetic nanoparticle temperature estimation. Med Phys. 2009; 36:1822–1829. [PubMed: 19544801]
61. Barrett T, Kobayashi H, Brechbiel M, Choyke PL. Macromolecular MRI contrast agents for imaging tumor angiogenesis. Eur J Radiol. 2006; 60:353–366. [PubMed: 16930905]
62. Orringer DA, Koo YE, Chen T, Kopelman R, Sagher O, Philbert MA. Small Solutions for Big Problems: The Application of Nanoparticles to Brain Tumor Diagnosis and Therapy. Clin Pharmacol Ther. 2009; 85:531–534. [PubMed: 19242401]
63. Peters D, Kastantin M, Kotamraju VR, Karmali PP, Gujraty K, Tirrell M, Ruoslahti E. Targeting atherosclerosis by using modular, multifunctional micelles. P Natl Acad Sci USA. 2009; 106:9815–9819.
64. Simberg D, Duza T, Park JH, Essler M, Pilch J, Zhang L, Derfus AM, Yang M, Hoffman RM, Bhatia S, Sailor MJ, Ruoslahti E. Biomimetic amplification of nanoparticle homing to tumors. P Natl Acad Sci USA. 2007; 104:932–936.
65. Johansson LO, Bjornerud A, Ahlstrom HK, Ladd DL, Fujii DK. A targeted contrast agent for magnetic resonance imaging of thrombus: implications of spatial resolution. J Magn Reson Imaging. 2001; 13:615–618. [PubMed: 11276107]
66. Sugahara KN, Teesalu T, Karmali PP, Kotamraju VR, Agemy L, Girard OM, Hanahan D, Mattrey RF, Ruoslahti E. Tissue-penetrating delivery of compounds and nanoparticles into tumors. Cancer Cell. 2009; 16:510–520. [PubMed: 19962669]
67. Jander S, Schroeter M, Saleh A. Imaging inflammation in acute brain ischemia. Stroke. 2007; 38:642–645. [PubMed: 17261707]

68. Rudd JH, Hyafil F, Fayad ZA. Inflammation imaging in atherosclerosis. Arterioscler Thromb Vasc Biol. 2009; 29:1009–1016. [PubMed: 19304673]
69. Neuwelt EA, Varallyay P, Bago AG, Muldoon LL, Nesbit G, Nixon R. Imaging of iron oxide nanoparticles by MR and light microscopy in patients with malignant brain tumours. Neuropath Appl Neuro. 2004; 30:456–471.
70. Varallyay P, Nesbit G, Muldoon LL, Nixon RR, Delashaw J, Cohen JI, Petrillo A, Rink D, Neuwelt EA. Comparison of two superparamagnetic viral-sized iron oxide particles ferumoxides and ferumoxtran-10 with a gadolinium chelate in imaging intracranial tumors. Am J Neuroradiol. 2002; 23:510–519. [PubMed: 11950637]
71. Kooi ME, Cappendijk VC, Cleutjens KB, Kessels AG, Kitslaar PJ, Borgers M, Frederik PM, Daemen MJ, van Engelshoven JM. Accumulation of ultrasmall superparamagnetic particles of iron oxide in human atherosclerotic plaques can be detected by in vivo magnetic resonance imaging. Circulation. 2003; 107:2453–2458. [PubMed: 12719280]
72. Schmitz SA, Taupitz M, Wagner S, Wolf KJ, Beyersdorff D, Hamm B. Magnetic resonance imaging of atherosclerotic plaques using superparamagnetic iron oxide particles. J Magn Reson Imaging. 2001; 14:355–361. [PubMed: 11599058]
73. Astalan AP, Ahrentorp F, Johansson C, Larsson K, Krozer A. Biomolecular reactions studied using changes in Brownian rotation dynamics of magnetic particles. Biosens Bioelectron. 2004; 19:945–951. [PubMed: 15128114]
74. Perez JM, Josephson L, O'Loughlin T, Hogemann D, Weissleder R. Magnetic relaxation switches capable of sensing molecular interactions. Nat Biotechnol. 2002; 20:816–820. [PubMed: 12134166]
75. Rauwerdink AM, Weaver JB. Measurement of molecular binding using the Brownian motion of magnetic nanoparticle probes. Appl Phys Lett. 2010; 96
76. Shellock FG, Kanal E, Gilk TB. Regarding the Value Reported for the Term"Spatial Gradient Magnetic Field" and How This Information Is Applied to Labeling of Medical Implants and Devices. Am J Roentgenol. 2011; 196:142–145. [PubMed: 21178059]
77. Schenck JF. Safety of strong, static magnetic fields. J Magn Reson Imaging. 2000; 12:2–19. [PubMed: 10931560]
78. Weizenecker J, Borgert J, Gleich B. A simulation study on the resolution and sensitivity of magnetic particle imaging. Phys Med Biol. 2007; 52:6363–6374. [PubMed: 17951848]
79. Saritas, EU.; Goodwill, PW.; Zhang, GZ.; Yu, W.; Conolly, SM. Safety Limits for Human- Size Magnetic Particle Imaging Systems. In: Borgert, TMBaJ, editor. Magnetic Particle Imaging. Lubeck, Germany: Springer Proceedings in Physics; 2012. p. 325-330.
80. Matthes R. I.C.N.-I.R. Pro, Medical magnetic resonance (MR) procedures: Protection of patients. Health Phys. 2004; 87:197–216. [PubMed: 15257220]
81. Weinberg IN, Stepanov PY, Fricke ST, Probst R, Urdaneta M, Warnow D, Sanders H, Glidden SC, McMillan A, Starewicz PM, Reilly JP. Increasing the oscillation frequency of strong magnetic fields above 101 kHz significantly raises peripheral nerve excitation thresholds. Med Phys. 2012; 39:2578–2583. [PubMed: 22559628]
82. Meikle SR, Kench P, Kassiou M, Banati RB. Small animal SPECT and its place in the matrix of molecular imaging technologies. Phys Med Biol. 2005; 50:R45–R61. [PubMed: 16264248]

- Magnetic Particle Imaging (MPI) is a new tracer imaging modality first presented in 2005
- MPI employs iron oxide (SPIO) contrast agents for kidney-safe angiography
- SPIOs in MPI generate positive, “bright blood” contrast, with no signal from tissue
- MPI already achieves fast, high-contrast angiograms with millimeter-scale resolutions
- MPI has great potential for stem cell tracking, cancer diagnosis, inflammation imaging

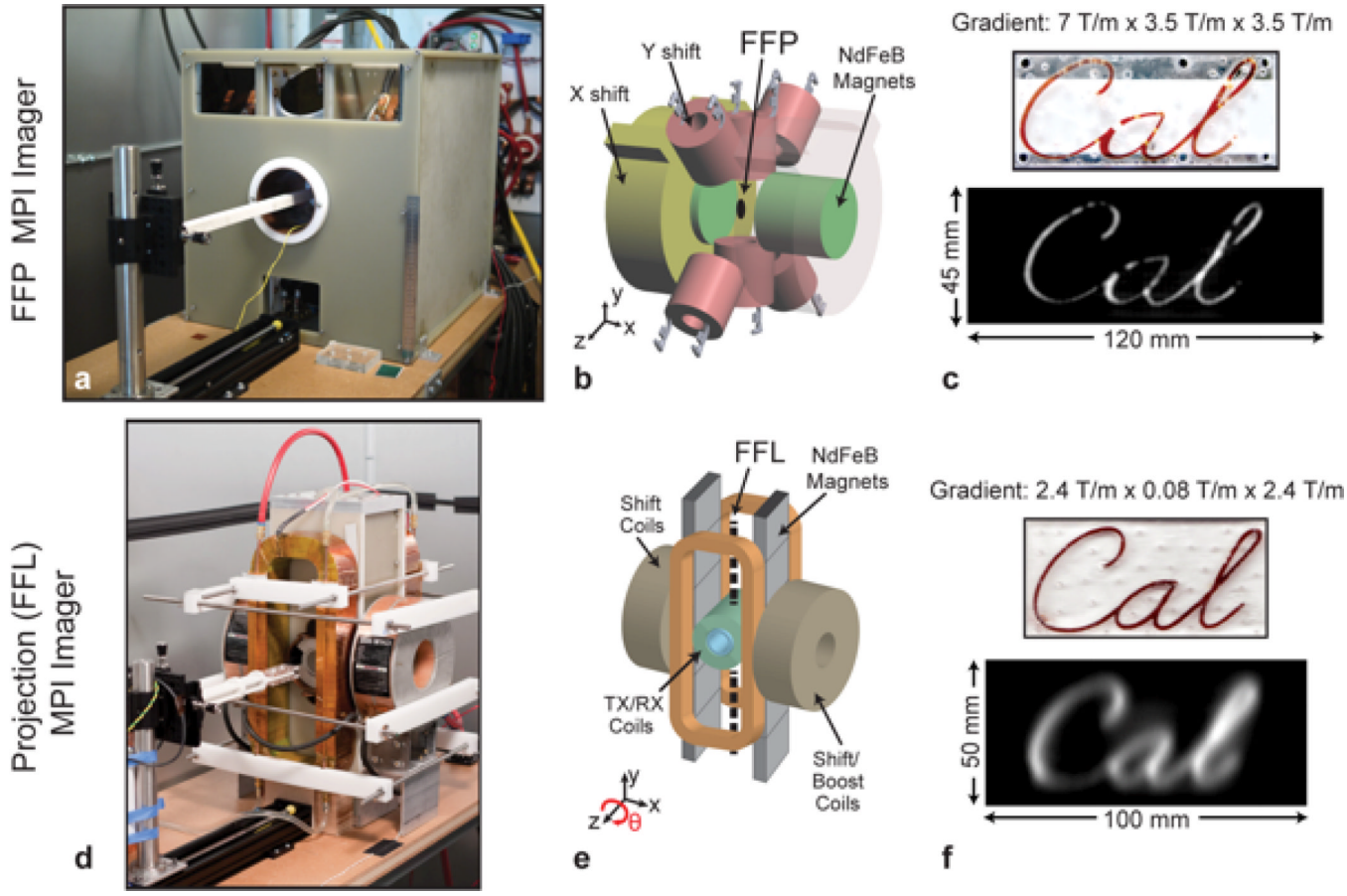

Figure 1.

X-space FFP and Projection (FFL) MPI imagers at UC Berkeley. **(a-b)** The FFP MPI imager's main field gradient is constructed using two opposed NdFeB permanent magnet cylinders, which produce a Field Free Point (FFP) at the magnet iso-center. **(c)** An MPI image of a "Cal" phantom filled with 10× diluted Resovist SPIO tracer taken using the FFP imager shows millimeter-scale resolution. **(d-e)** The projection (FFL) MPI imager's main field gradient is constructed using two opposed NdFeB permanent magnet assemblies to produce a Field Free Line (FFL) along the instrument's *y*-axis. **(f)** An MPI image of a similar "Cal" phantom filled with 10× diluted Resovist tracer taken using the projection scanner. This image has three times lower resolution than (c) due to a weaker magnetic field gradient, but was otherwise taken using nearly identical acquisition parameters.

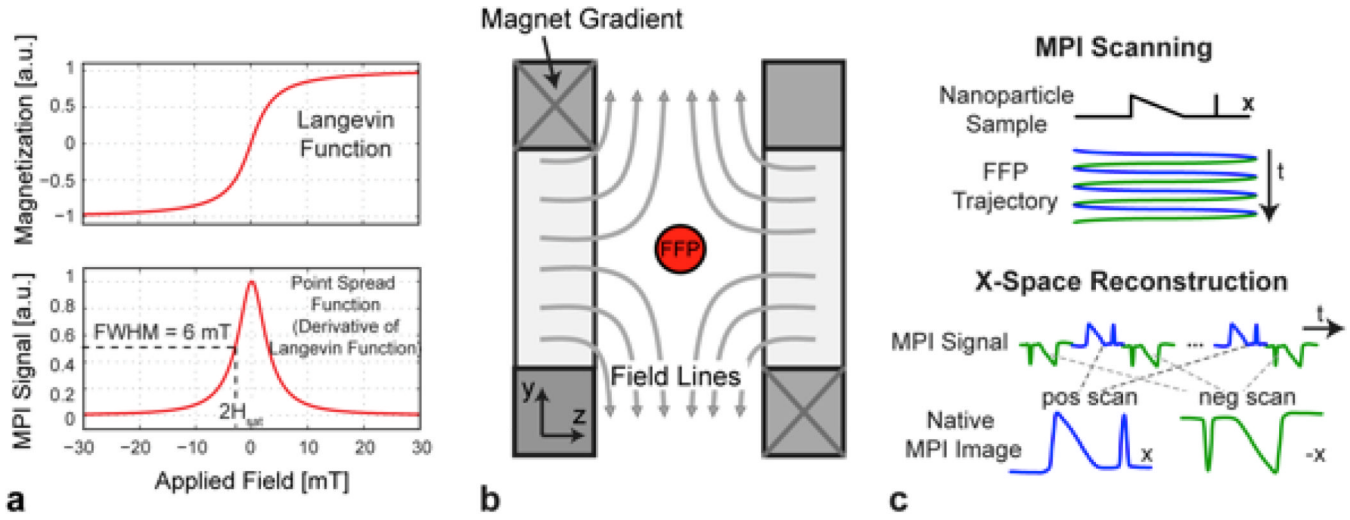

Figure 2.

Principles of x-space MPI imaging. **(a)** SPIO magnetization, characterized by a Langevin function, is nonlinear with the applied magnetic field and converges to saturation above a certain threshold. This nonlinear magnetization response determines the point spread function (PSF) in MPI. The simulated PSF with a FWHM of 6 mT is for a log-normally distributed iron oxide nanoparticle with diameter 20 +/− 2.5 nm. For a 6 T/m gradient field, this FWHM corresponds to 1 mm resolution. **(b)** Two permanent magnets create a strong magnetic field gradient and a sensitive point, called the field free point (FFP). Only the SPIOs in the instantaneous location of the FFP create an MPI signal. **(c)** To cover the imaging field-of-view, the FFP is moved rapidly in a trajectory across the imaged volume. Using X-space reconstruction, we grid the MPI signal to the instantaneous position of the FFP to form a native MPI image. Figure adapted from [23].

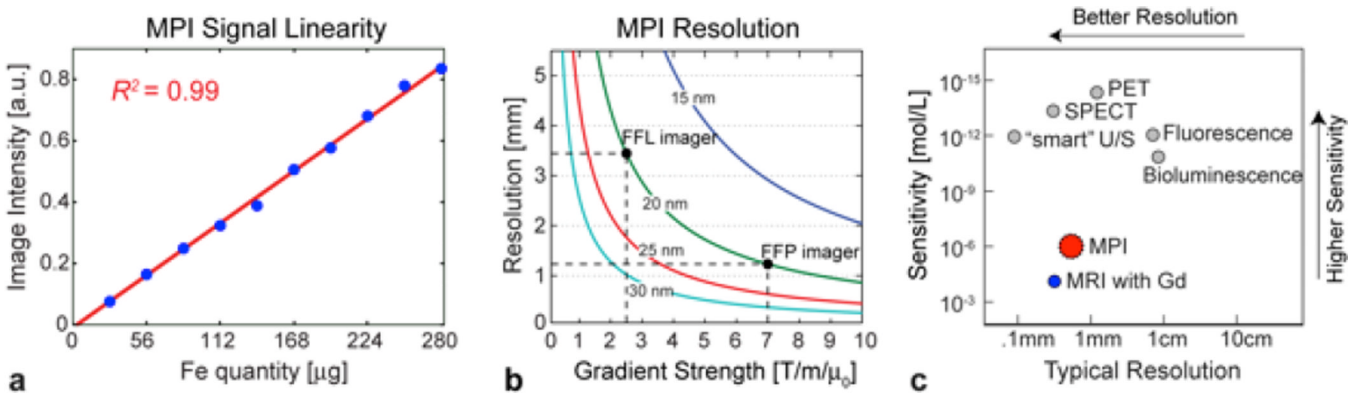

Figure 3.

(a) The signal in MPI is perfectly linear ($R^2 = 0.99$) with iron quantity, i.e., the input nanoparticle quantity. **(b)** Theoretical resolution of MPI improves cubically with the nanoparticle size and linearly with the gradient strength. The resolutions of our two MPI scanners in Fig. 1 are marked for a 20 nm particle size. The FFP MPI imager and the Projection (FFL) imager feature 7 T/m/ $_0$ and 2.4 T/m/ $_0$ gradient strengths, respectively. **(c)** Comparison of tracer and contrast agent sensitivities in small animal (pre-clinical) imaging modalities, and where we expect MPI to be in the next couple of years. MPI compares well to existing imaging techniques and is a promising competitor. Here"smart" U/S refers to ultrasound with micro-bubbles. Subfigure (b) adapted from [23], and subfigure (c) adapted from [82].

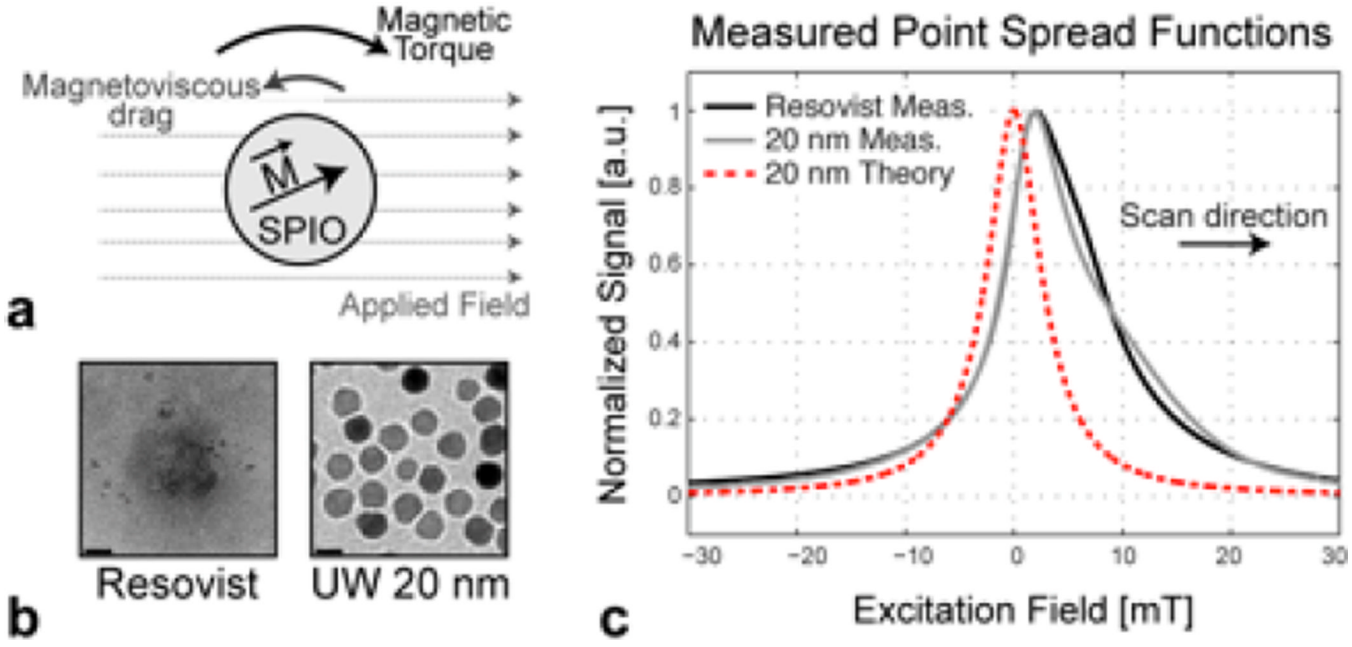

Figure 4.

Physics of superparamagnetic iron oxide (SPIO) nanoparticles. **(a)** For bigger SPIO nanoparticles, the ability to rotate to align their magnetization with the applied field is slowed down by magnetoviscous drag. **(b)** TEM images of a commercially available contrast agent, Resovist, and tailored nanoparticles with 20 nm mean iron oxide core diameter synthesized at the University of Washington (Scale bars = 20 nm) [34]. **(c)** Point spread functions (PSFs) for Resovist and 20-nm UW particles, measured using x-space MPI relaxometry [24]. The tailored 20-nm UW particles are already performing at the level of Resovist in terms of their FWHM resolution, but are more efficient because they produce higher MPI signal for the same iron content [37]. Note that the PSFs for both Resovist and 20-nm UW particles demonstrate lagging due to relaxation effects from magnetoviscous drag [24]. Figure adapted from [23].

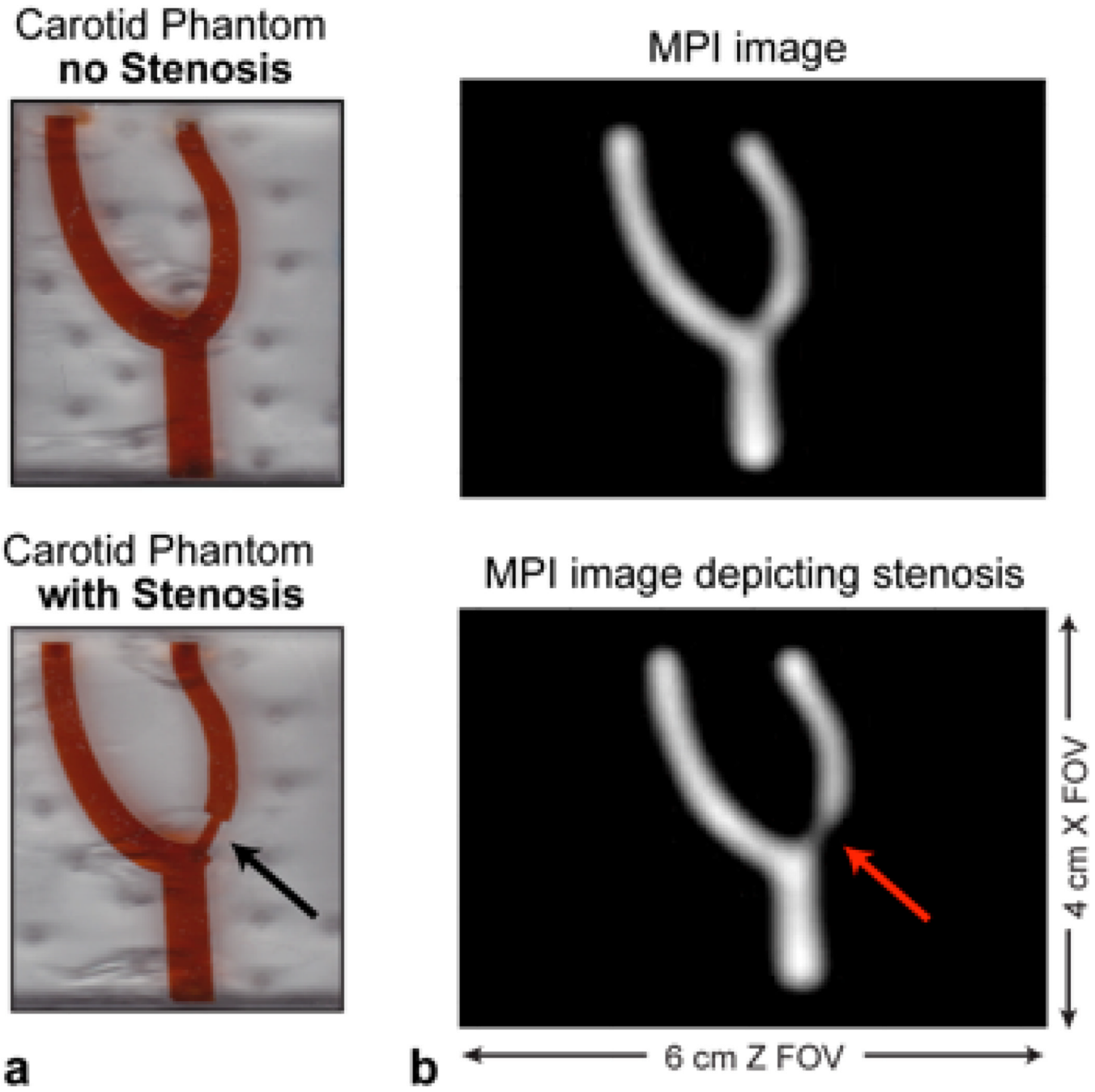

Figure 5.
MPI images of "carotid artery" phantoms, mimicking a healthy (top) and an occluded (bottom) internal carotid artery. MPI image successfully captures the stenosis in the phantom, depicted with a reduced brightness and a narrowing. **(a)** Photos of carotid artery phantoms made of acrylic with a 3 mm thickness for the branches and a 4 mm thickness for the common artery (about 75% the size of typical carotid artery in humans). The channels were injected with 20× diluted Resovist tracer. **(b)** MPI images were acquired on our high-resolution FFP MPI scanner, and mildly deconvolved with a Wiener filter. FOV: 4.5 cm by 4.5 cm by 6.2 cm. Scan time: 141 seconds.

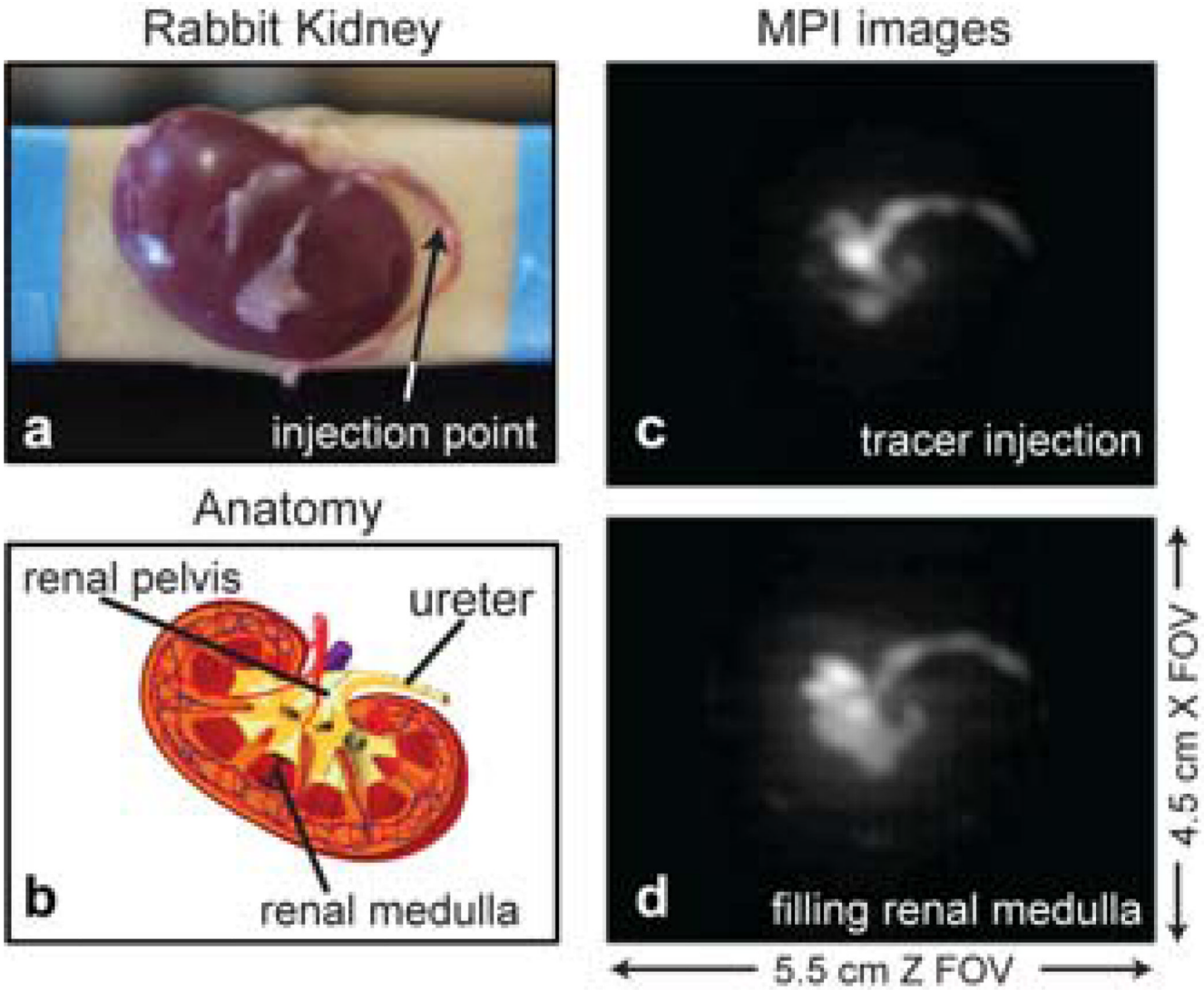

Figure 6.

MPI images demonstrating imaging of *ex vivo* rabbit kidney on the high-resolution FFP MPI scanner at UC Berkeley. **(a)** *Ex vivo* rabbit kidney photograph and **(b)** rabbit kidney anatomy for reference. **(c)** MPI image following injection of 3X diluted Resovist tracer into ureter. Visible is the ureter and the renal pelvis. **(d)** Injecting DI water washes the Resovist tracer further into the kidney. The MPI image shows that the tracer has now entered the renal medulla. FOV: 5.5 cm × 4.5 cm. Scan time: 2 minutes per image, including all robot movement.

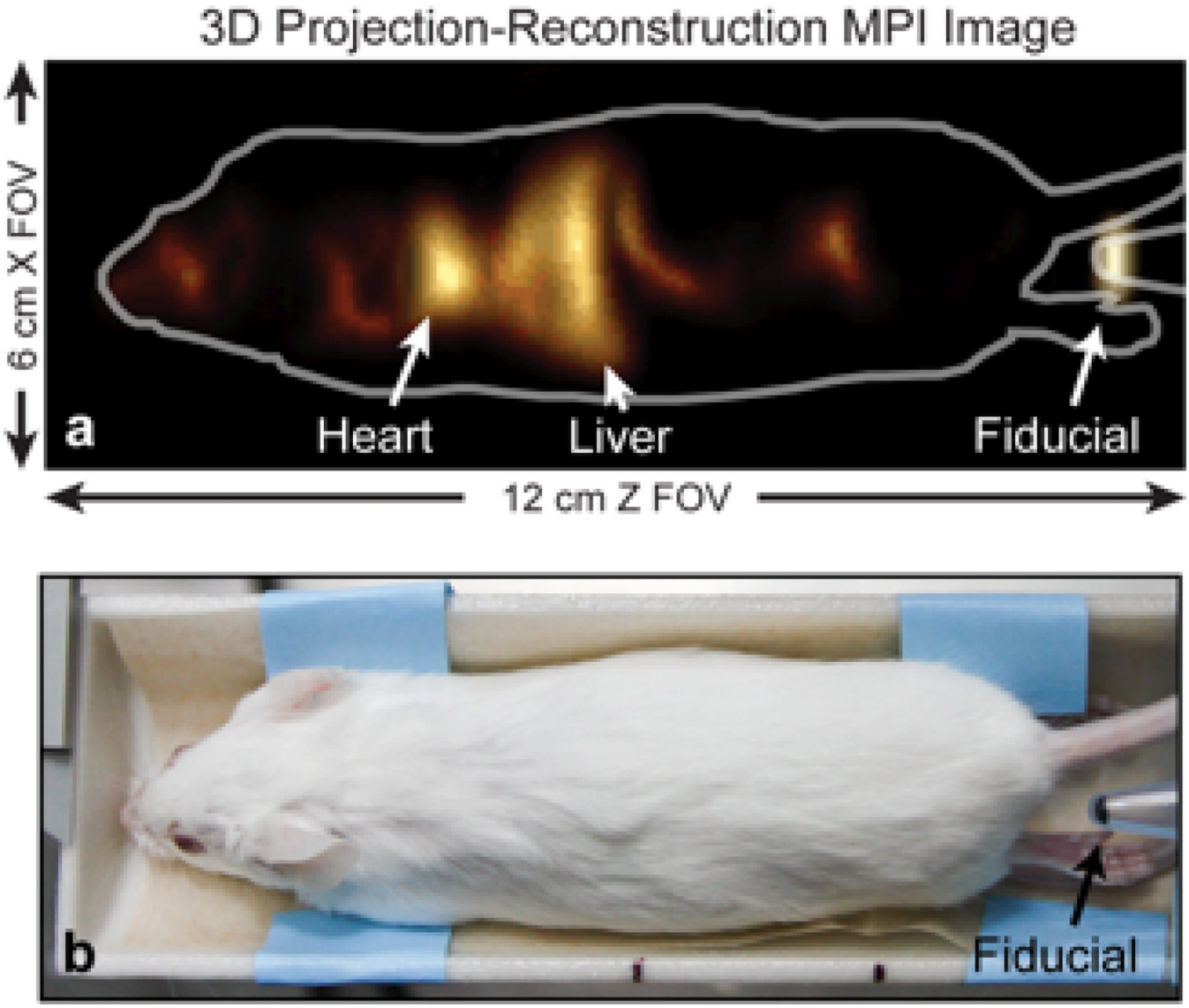

Figure 7.

3D projection reconstruction MPI image showing the Resovist tracer flowing to the heart and filtering in the liver of a mouse. **(a)** The volume-rendered MPI image and **(b)** the photo of the mouse injected with 100 L undiluted Resovist via tail vein and sacrificed 30 s post-injection. Imaging was performed with the Projection (FFL) MPI scanner with 180 projections, 3 min per projection acquisition time, FOV: 12 cm × 6 cm.

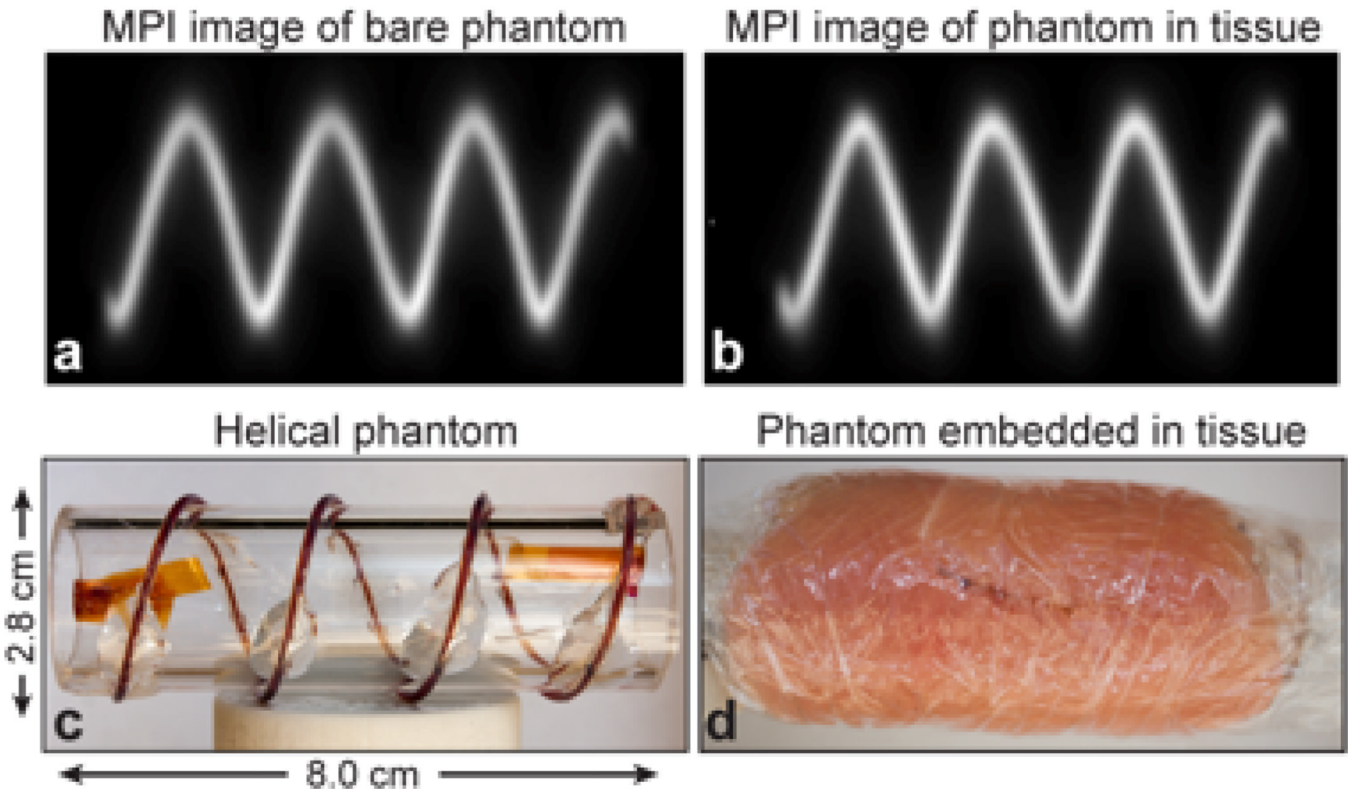

Figure 8.

3D MPI experiment demonstrating no depth attenuation or tissue contrast. **(a-b)** Projection Reconstruction 3D MPI images show no attenuation with depth for the phantom embedded in tissue, nor any tissue contrast. **(c)** Helical phantom filled with SPIOs and **(d)** the same phantom embedded in animal (*Meleagris Gallopavo*) tissue. Images were acquired the UC Berkeley Projection (FFL) MPI scanner with 60 projections, volume reconstructed using Projection Reconstruction, and then displayed as a maximum intensity projection. Comparing the two images, there are no qualitative differences and a negligible change in signal level. FOV: 12 cm × 6 cm, 2 averages, 21 s per projection acquisition time, 10× diluted Resovist (50 mM) injected in 0.8 mm ID tubing wrapped around a 2.6 cm OD acrylic tube.

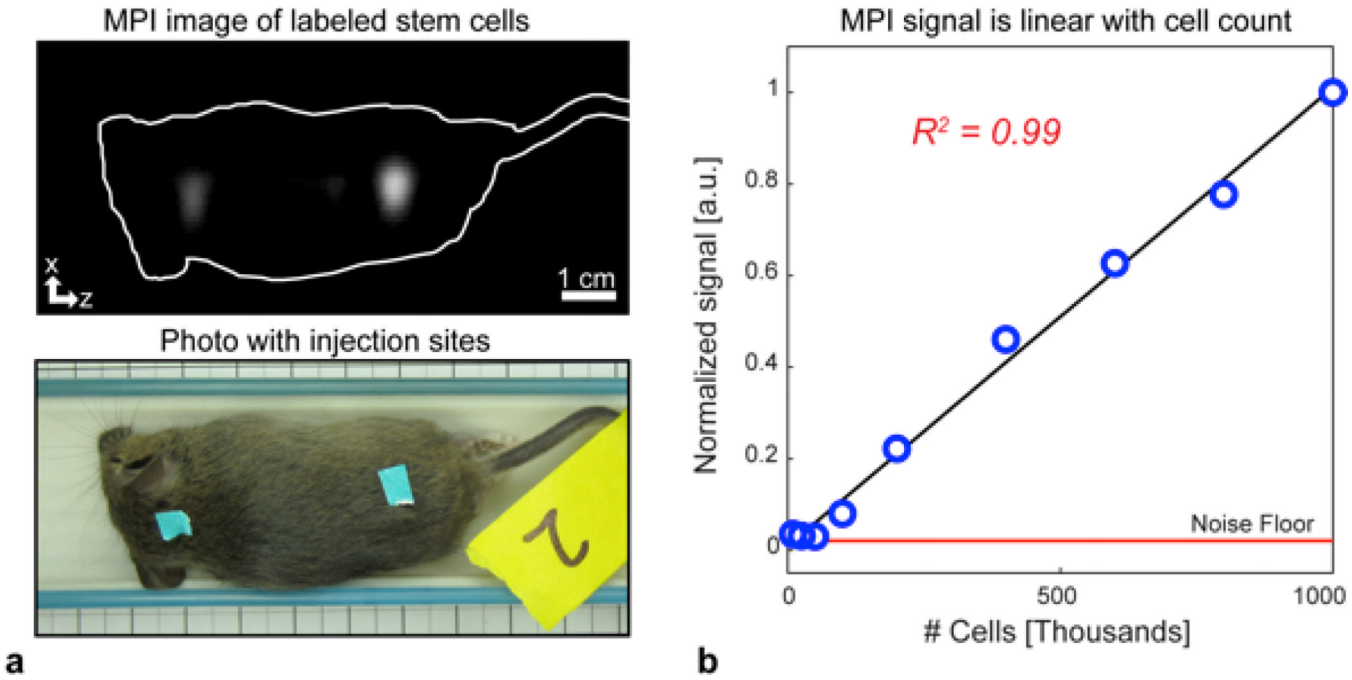

Figure 9.

Stem cell imaging with MPI. **(a)** Projection MPI image of two injections of hESC-derived cells (1×10^5 cells on the left vs. 2×10^5 cells on the right site) introduced subdermally into a postmortem mouse (injection sites marked in cyan in the photo). The ratio of signal intensities between the right and left injection regions in the MPI image was found to be 2.1. Image acquisition time was 3 minutes total with FOV of 5×10 cm and 16 averages. **(b)** Plot of MPI signal intensity vs. number of stem cells in scanner, demonstrating excellent linear fit ($R^2 = 0.99$). MPI images were acquired for 9 stem cell populations ranging from 1×10^4 to 1×10^6 cells and compared for maximum signal intensity. Our current stem cell detection threshold (i.e., the noise floor) is limited by system interference, and is approximately 1×10^4 cells in our prototype system.

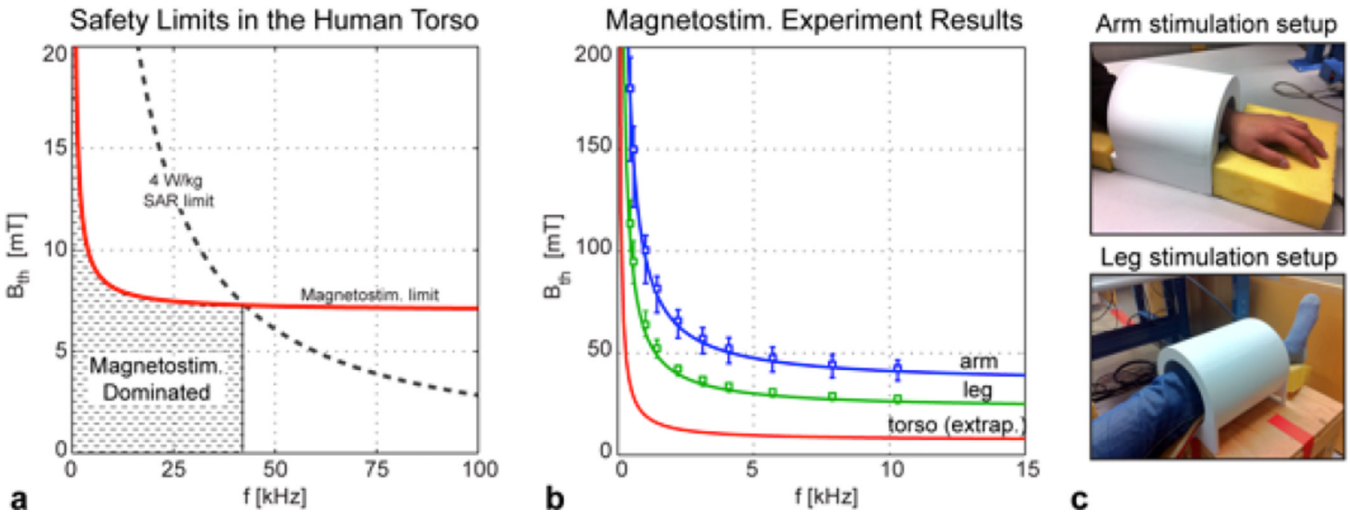

Figure 10.

Safety limits for human-size MPI scanners. **(a)** Magnetostimulation is the dominant safety concern for the excitation field in MPI, which typically operates around 25 kHz. The SAR threshold curve was calculated for a continuous (i.e., 100% duty cycle) sinusoidal magnetic field and a 4 W/kg limit. **(b)** Human subject experiments results for magnetostimulation in the arm and leg. Peak magnetic field amplitudes for the median stimulation thresholds and the 30th-70th percentile are shown (N = 20 and N = 17 for the arm and leg experiments, respectively). The magnetostimulation thresholds for the human torso were extrapolated using the results in the arm and the leg, and assuming a radius of r = 20 cm (typical radius of human torso). **(c)** Setups for testing the magnetostimulation thresholds in the human arm and leg. Figure adapted from [79].

Table 1

Comparison of key differences between Fourier-domain scanning in *k*-space MRI and spatial-domain scanning in x-space MPI. Note that this comparison assumes a field-free point (FFP) MPI scanner and spherical SPIO nanoparticles.

	***k*-space MRI**	**x-space MPI**
Imaging Equation	Instantaneous *k*-space scanning location controlled by the integral of the gradient waveforms	Instantaneous x-space scanning location determined by the position of the field-free point (FFP)
Image Resolution	Determined by the maximum extent of *k*-space sampled. Can be curtailed by relaxation, diffusion, or poor SNR.	Determined by the SPIO particle's Langevin curve and the applied field gradient strength. Can be curtailed by relaxation or poor SNR. In theory, improves cubically with particle size.
Image Aliasing	Prevented by sampling in *k*-space finer than 1/FOV.	Not a primary concern in MPI due to scanning in x-space.
Magnetic Field Homogeneity	Magnetic field (B_0) distortions as small as parts-per-million can cause significant signal dropouts.	A minor concern in MPI. No magnets in FFP MPI require better than 5% field homogeneity.
Averaging for SNR	Imaging in *k*-space greatly improves SNR. All time spent acquiring data contributes SNR equally to each voxel in the image.	Imaging in x-space allows us to focus our time on voxels that contain SPIOs. Time spent acquiring data contributes SNR *only* to the current voxel.